Materials and Design 109 (2016) 162–170

Contents lists available at ScienceDirect

Materials and Design

journal homepage: www.elsevier.com/locate/matdes

Carbon nanofibers as nanoreactors in the construction of PtCo alloy carbon core-shell structures for highly efficient and stable water splitting

XinRong Liu [a], Ming Zhang [a,b,*], TingTing Yang [a], LiNa Wang [b], Han Zhu [a,b,*], ShunLi Wang [c], MingLiang Du [a,b]

[a] Department of Materials Engineering, College of Materials and Textiles, Zhejiang Sci-Tech University, Hangzhou 310018, PR China
[b] Key Laboratory of Advanced Textile Materials and Manufacturing Technology, Zhejiang Sci-Tech University, Ministry of Education, Hangzhou 310018, PR China
[c] Department of Physics, Center for Optoelectronics Materials and Devices, Zhejiang Sci-Tech University, Hangzhou 310018, PR China

HIGHLIGHTS

- PtCo alloy carbon core-shell nanostructures with nitrogen doping were synthesized.
- Carbon nanofibers served as nanoreactors.
- The PtCo alloy carbon exhibits high HER and OER activity and high stability.
- The OER activities originate from the conductivity of NCNF and the PtCo alloy.

GRAPHICAL ABSTRACT

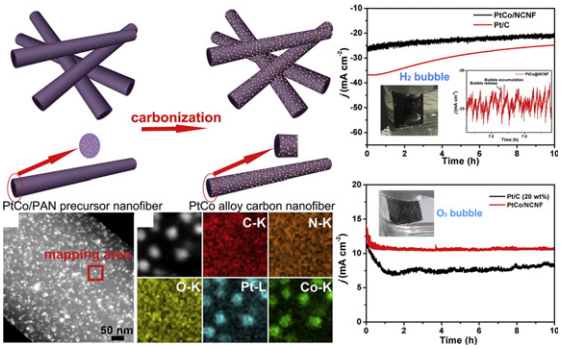

ARTICLE INFO

Article history:
Received 23 May 2016
Received in revised form 5 July 2016
Accepted 8 July 2016
Available online 14 July 2016

Keywords:
PtCo alloy
Carbon nanofibers
Nanoreactors
Hydrogen evolution reaction
Oxygen evolution reaction

ABSTRACT

Carbon nanofibers served as nanoreactors for the design and construction of PtCo alloy carbon core-shell nanostructures with nitrogen doping (PtCo/NCNF) through a combination of electrospinning and nitrogen doping treatments. The PtCo/NCNF hybrid consists of PtCo alloy nanoparticles surrounded by a few of N-doped carbon layers, demonstrating a typical core-shell structures. The PtCo/NCNF hybrid can both served as electrode materials for electrocatalytic water splitting including hydrogen evolution reaction (HER) and oxygen evolution reaction (OER). For the HER performance, the PtCo/NCNF exhibits very small onset potential of 20 mV, an overpotential of 50 mV at a j (vs RHE) = 10 mA cm^{-2} and Tafel slope of 30 mV dec^{-1}. The PtCo/NCNF hybrid also exhibits high OER activity with an onset potential of 310 mV, an overpotential of 400 mV at a j of 10 mA cm^{-2} and a small Tafel slope of 76 mV dec^{-1}. The high catalytic activities of PtCo alloy for HER and OER originate from the 3D hierarchical structures, well-dispersed PtCo alloy, high conductivity of NCNF, protection from the carbon-encapsulated structure, and the introduction of nitrogen.

1. Introduction

Water splitting has been hailed as a promising candidate to meet the increasing demands for clean and sustainable energy on the global scale. Electrocatalytic water splitting consists of the hydrogen evolution reaction (HER) and the oxygen evolution reaction (OER) [1]. One of the

* Corresponding authors at: Department of Materials Engineering, College of Materials and Textiles, Zhejiang Sci-Tech University, Hangzhou 310018, PR China.
E-mail addresses: zhangming@zstu.edu.cn (M. Zhang), zhuhanfj@163.com (H. Zhu).

http://dx.doi.org/10.1016/j.matdes.2016.07.060
0264-1275/

important approaches is to develop highly efficient and durable electrocatalysts that can substantially expedite the kinetics of HER and OER process [2,3]. Therefore, to improve the energy efficiency, an high-performance electrocatalyst is essential for reducing the overpotentials of electrodes, promoting the reaction kinetics, and enhancing the specific activity. However, compared to the HER, the OER process is harsh and kinetically sluggish because of its thermodynamically and kinetically demanding process involving four sequential proton-coupled electron transfer steps and the oxygen-oxygen bonding formation [3]. The four sequential proton-coupled electron transfer steps for OER process leads to slower kinetics and relatively higher overpotentials [2–5]. Co-based electrocatalysts, such as CoP, Co_3O_4 and CoS_2 have been known as active OER catalysts, and considerable efforts has been made to develop advanced Co-based nanostructures for improving the OER activity and stability [6–11].

Notwithstanding significant progress, there are only a few catalysts that are able to catalyze both HER and OER process. Recently, a type of precious-metal alloy with transition metal (Co, Mn, etc.) [12,13] and nonmetal catalyst (graphitic carbon, N-doped graphitic carbons, etc.) [14] have been employed as an effective co-electrocatalyst for HER or OER. In this regard, it is of great interest to introduce a certain amount of Pt into Co phase to generate PtCo alloy for the overall water splitting. The PtCo alloy exhibits good catalytic activity along with good durability due to the modification of the Pt electronic structure. Wang and coworkers reported cobalt-embedded N-doped carbon nanotubes (CNTs), exhibiting both high oxygen reduction reaction (ORR) and OER activity [14]. The high catalytic activity of cobalt-embedded N-doped CNTs is thought to be facilitated by the combination of the embedded cobalt, the N-doped carbon, and the CNTs substrate. It is reported that metal embedding has been found to be conducive to protecting the metal nanoparticles from dissolution, migration, detachment and coalescence by the electrolyte, resulting in high long-term stability [15].

Recently, Du et al. group have reported the novel fabrication of carbon nanofibers (CNF) supported noble metal nanoparticles, transitional metal dichalcogenides nanoplates and core-shell nanostructures [15–18]. The nanocrystal/carbon nanofibers systems exhibit superior electrocatalytic activity for water splitting. Three-dimensional (3D) nanomaterials with hierarchical structure have been widely designed for the electrochemical reactions, such as HER, OER and ORR [19–22]. Compared with bulk solid structures, the complex hierarchical structures endow materials with high specific surface areas, which can facilitates diffusion of active species and accelerates subsequent surface reactions [20–22]. The one-dimensional (1D) nanostructures of CNF can provide more contact surfaces between supported catalysts and electrolyte. The interconnected 3D architecture of CNF induces large interfaces and interstices of the electrolyte and the nanocrystal surfaces, which provide rapid electron transport and fast gas diffusion [20,22]. In addition, the 3D architecture of CNF also can promote the release of evolved gas bubbles, which are benefit for the electrode kinetics and catalytic performance [23]. Meanwhile, the introduction of nitrogen into carbon material not only can promote electronic transfer but also provide more active sites for both the OER and ORR [24–26]. It is of great interest to fabricate hierarchical 3D structures integrated with PtCo alloy and CNF, serving as promising materials for both HER and OER in electrocatalytic water splitting.

Herein, inspired by the superiority of PtCo alloy, N-doped carbon and enhanced durability of metal embedding, the CNF were used as a nanoreactor to synthesize PtCo alloy carbon core-shell nanostructures with nitrogen doping (PtCo/NCNF) through a combination of electrospinning and nitrogen doping treatments. Small sized PtCo alloy carbon core-shell nanoparticles were uniformly dispersed throughout the whole CNF. The PtCo/NCNF hybrid consists of PtCo alloy nanoparticles surrounded by a few of N-doped carbon layers, demonstrating a typical core-shell structures. The PtCo/NCNF hybrid can both served as electrode materials for HER and OER. For the HER performance, the novel nanomaterials exhibit very small onset potential of 20 mV, overpotentials at a j (vs RHE) of 10 mA cm^{-2} of 50 mV and Tafel slope of 30 mV dec^{-1}, which are better than the commercial Pt/C (20 wt%) catalysts (onset potential of 27 mV and overpotentials at a j (vs RHE) of 10 mA cm^{-2} of 59 mV) and PtCo/NCNF without NH_3 treatment (onset potential of 34 mV and overpotentials at a j (vs RHE) of 10 mA cm^{-2} of 68 mV). In addition, the PtCo/NCNF hybrid also exhibits high OER activity with an onset potential of 310 mV, an overpotential of 400 mV at a j (vs RHE) of 10 mA cm^{-2} and a small Tafel slope of 76 mV dec^{-1}, which are also better than PtCo/CNF (onset potential of 340 mV, an overpotential of 520 mV at a j (vs RHE) of 10 mA cm^{-2} and Tafel slope of 83 mV dec^{-1}). The PtCo/NCNF membrane can be directly used as electrodes for HER and OER, demonstrating superior stability in acid and alkaline conditions after continuous operation for 10 h. The high catalytic activities of PtCo alloy for HER and OER originate from the 3D hierarchical structures, well-dispersed PtCo alloy, high conductivity of CNF, protection from the carbon-encapsulated structure, and the introduction of nitrogen.

2. Experimental

2.1. Materials

Chloroplatinic acid ($H_2PtCl_6 \cdot 6H_2O$, 99.9%) and dimethylformamide (DMF, 99.5%) were procured from Shanghai Civi Chemical Technology Co., Ltd. Cobalt chloride hexahydrate ($CoCl_2 \cdot 6H_2O$) and potassium hydroxide (KOH) were supplied by Aladdin Co., Ltd. Polyacrylonitrile (PAN, $M_w \approx 1.4 \times 10^5$, copolymerized with 10 wt% methyl acrylate) was purchased by Sinopec Shanghai Petrochemical Co., Ltd. Ultrapure water (Milli-Q) was used throughout the experiments. All were used as received without further purification.

In a typical procedure, 0.15 g of $CoCl_2 \cdot 6H_2O$ and 0.15 g of $H_2PtCl_6 \cdot 6H_2O$ were co-dissolved in 22 mL of a PAN/DMF solution with a mass fraction of 10% PAN. Thereafter, the homogeneity of the three-component mixture was obtained by vigorously stirring of the mixture at 80 °C for 3 h. Afterward, the mixture was transferred to a syringe with a stainless copper needle at the tip. The needle was connected to a high voltage power supply to get a voltage of 15 kV, the needle-to-collector distance was about 12 cm, and the flow rate of the precursor solution was 0.6 mL h^{-1}.

Under these conditions, the homogeneous PtCo/PAN nanofibrous membrane were obtained at room temperature. The direct growth of the PtCo/NCNF hybrid was carried out in a home-built chemical vapor deposition (CVD) furnace. The as-collected PtCo/PAN nanofibrous mats were placed in a ceramic boat located at quartz tube in the center of the heating zone of the furnace. Next, the PtCo/PAN nanofibrous mats were heated in air from room temperature at a temperature ramp of 5 °C min^{-1} to 230 °C and maintained for 6 h. After the stabilization process, the nanofiberous mats were continue to heat up with the feeding of Ar (150 sccm) at ambient pressure. When the temperature reached 400 °C, the NH_3 (10 sccm) gas was introduced. After 2 h, the NH_3 gas was then turned off, while the furnace temperature was heated up to 1000 °C and the temperature was held constant for 8 h. The samples were cooled to room temperature naturally under the protection of flowing Ar. For reliable comparison, the PtCo/CNF, NCNF and CNF were prepared similarly as a control.

2.2. Characterization

Field-emission scanning electron microscopy (FE-SEM) images were recorded on the JSM-6700F (JEOL, Japan) at high vacuum with an accelerating voltage of 3 kV. Transmission electron microscopy (TEM) images, high-resolution TEM (HRTEM) and selected-area electron diffraction (SEAD) were taken using a JSM-2100 transmission electron microscope (JEOL, Japan) at an acceleration voltage of 200 kV. The high-angle annular dark field scanning TEM (HAADF-STEM), STEM mapping, and line-scan energy dispersive X-ray spectroscopy (EDX) were taken with a STEM (Tecnai G2 F30S-Twin, Philips-FEI) operating

at 300 kV. The X-ray diffraction (XRD) analysis was carried out on a Bruker AXS D8 DISCOVER X-ray diffractometer with Cu K_α radiation ($\lambda = 1.5406$ A°) at a scanning rate of 0.02° 2θ s^{-1} in the 2θ range of 10–90°. X-ray photoelectron spectra (XPS) were performed on an X-ray photoelectron spectrometer (Kratos Axis Ultra DLD) with an aluminum (mono) K_α source (1486.6 eV). The aluminum K_α source was operated at 15 kV and 10 mA.

2.3. Electrochemical characterization

To prepare the working electrode, glassy carbon electrode (GCE, 3 mm diameter) was polished with 1.0, 0.3 and 0.05 μm alumina slurry, and thoroughly washed before surface modification. 3 mg catalyst was dispersed in 1 mL of 3:1 (volumetric ratio) water/isopropanol mixed solvent with 20 μL of Nafion solution (5 wt%) under ultra-sonication for 30 min until a homogeneous ink formed. The Nafion solution was used as a proton conducting binder to ensure good adhesion onto the electrode. Thereafter, 5 μL of catalyst ink was dropped onto a GC disk electrode using a micropipette, and then drying at room temperature (loading 212.3 μg cm^{-2}). Moreover, the as-prepared catalyst film was stored in a desiccator at room temperature before use. As a control, bare GCE that has been polished and cleaned was also dried for electrochemical measurement.

The electrochemical measurements were performed on a CHI660E workstation (Shanghai Chenhua, Shanghai) in a standard three-electrode cell. A modified GCE, a Pt wire and a saturated calomel electrode (SCE) were served as the working electrode, counter electrode and reference electrode in 0.5 M H_2SO_4 and 1 M KOH electrolytes, respectively. All the potentials were referenced to a reversible hydrogen electrode (RHE) by adding a value of (0.218 + 0.059 × pH) V. Prior to the electrochemical testing, a flow of N_2 was maintained for at least 15 min to remove the dissolved oxygen. The catalyst was first subject to cyclic voltammetry (CV) scans between 0 and 1.20 V vs the RHE at a scan rate of 100 mV s^{-1} with a continuous N_2 flow until a stable CV was obtained. Then, linear sweep voltammetry (LSV) polarization curves were performed at scan rate of 1 mV s^{-1} and all the polarization curves were iR-compensation. The accelerated stability test was performed by potential cycling between −0.2 and 1.0 V vs RHE at a sweep rate of 100 mV s^{-1} for 1000 cycles. At the end of the cycles, the resulting electrodes were used for polarization curves at a scan rate of 1 mV s^{-1}. The stability test of the PtCo/NCNF were also used a typical three electrode system. The PtCo/NCNF membrane was tailored into a neat square (1 × 1 cm) and directly utilized as the working electrode, and the current-time response was monitored by chronoamperometric measurements in 0.5 M and 1 M KOH electrolyte for 10 h. All measurements were performed at room temperature.

3. Results and discussion

After reducing Pt and Co precursor with carbon species in Ar/NH_3 atmosphere at high temperature, the former PtCo/PAN nanofibers convert into PtCo alloy carbon core-shell structures in NCNF. Fig. 1a and b show that the as-synthesized small sized PtCo alloy nanoparticles (NPs) are

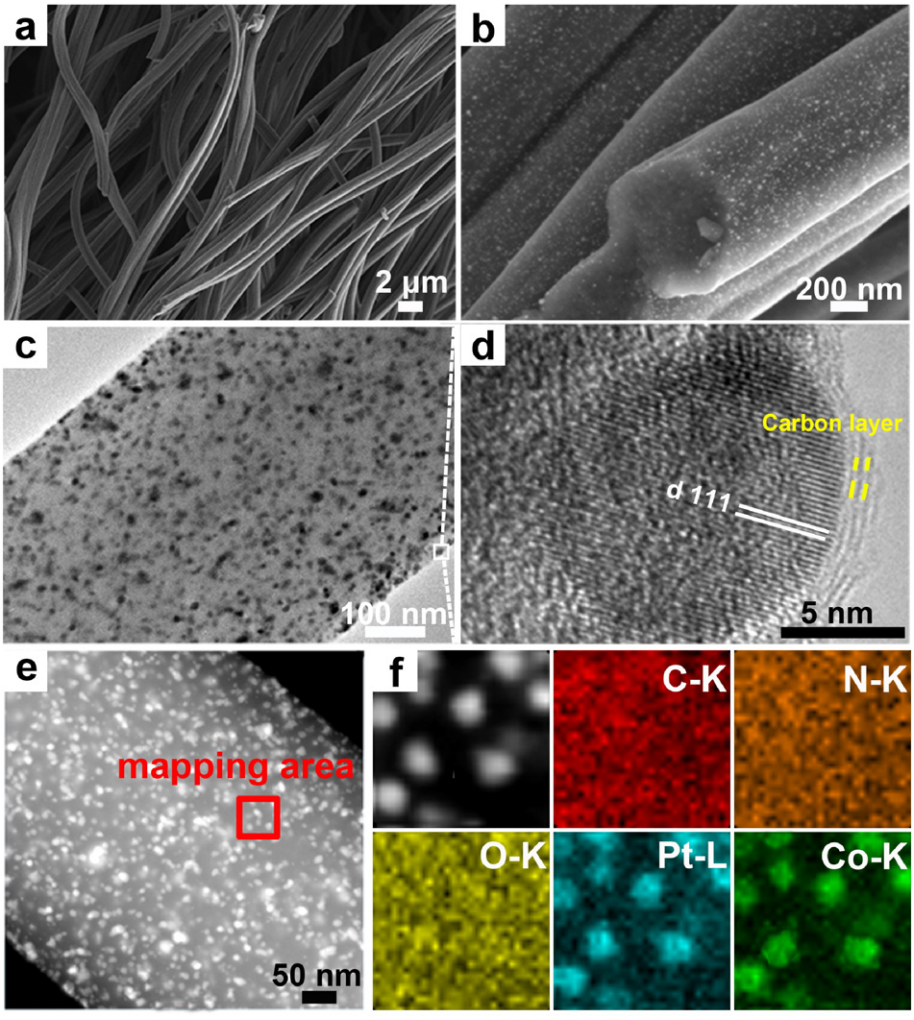

Fig. 1. (a, b) FESEM, (c) TEM, (d) HRTEM and (e) HAADF-STEM images of PtCo/NCNF hybrid nanostructure; (f) corresponding STEM-EDS element mapping images of PtCo/NCNF.

uniformly dispersed in N-doped CNF. The PtCo alloy NPs with an average diameter of 8.9 nm are uniformly embedded in the carbon matrix, as shown in Fig. 1c. It is reported that the Co NPs tend to grow up to larger size under thermal reduction [27]. As control, the Co/CNF were also prepared and as shown in Fig. 2a and b, the size of Co NP embedded in CNF is about 20 nm, demonstrating the well control in size by CNF. For the PtCo/CNF without NH_3 treatment, the PtCo alloy exhibit average diameter of 10.9 nm, as shown in Fig. 2c and d. After the NH_3 treatment during the growth process of PtCo alloy in NCNF, the PtCo alloy NP only exhibit an average diameter of 8.9 nm, indicating that the reduction atmosphere would help the NCNF to restrict the growth of PtCo alloy to larger sizes.

The TEM image in Fig. 1c also shows the well-dispersed PtCo alloy NP in NCNF. The HRTEM image in Fig. 1d clearly exhibits the core-shell nanostructures with PtCo NPs as the cores and graphitic carbon as the shells. The PtCo alloy NP displays continuous lattice fringes with a spacing of 0.23 nm, corresponding to the (111) plane of face-centered-cubic crystalline PtCo [27]. Notably, the PtCo alloy NPs were surrounded by a few graphitic carbon layers, where the inter-spacing of the carbon layers was 0.32 nm, attributing to the (002) planes of carbon (Fig. 1d). The formed PtCo alloy in NCNF could act as catalyst for the graphitization of the surrounded carbon, leading to the formation of PtCo alloy carbon core-shell structures. This structure would be advantageous for the stability of catalysts because the graphitic carbon layer is expected to keep the PtCo alloy NPs from aggregating or peeling off upon electrochemical cycling [1].

Furthermore, the alloy structure of PtCo NPs was verified via HAADF-STEM (Fig. 1e). The HAADF-STEM image of PtCo/NCNF displays the carbon, nitrogen, platinum, cobalt and oxygen elements. The complete overlapping of Pt and Co elements in the individual NPs implies an atomic mixture of Pt and Co without obvious phase segregation, which is in accordance with the mapping area of the PtCo alloy NPs in Fig. 1f. In addition, the nitrogen element was evenly distributed with the carbon element, demonstrating that the nitrogen element was uniformly doped into the carbon matrix. Fig. 3a and b represents the line scan STEM-EDX spectra across two PtCo alloy NPs. The resulting profile reveals that the consistent relative intensity of both Pt and Co in the two NPs, confirming the formation of a PtCo alloy structure. The EDS spectra of the PtCo/CNF and PtCo/NCNF hybrid membranes display the element atomic ratio of C, N, O, Pt and Co, as shown in Fig. 3d and c. The PtCo/NCNF possess higher N atomic ration about 2.59% than that of PtCo/CNF (0.78%), indicating the more N contents and doping in carbon matrix after NH_3 treatment.

The crystalline structure of the PtCo/NCNF hybrid was investigated by XRD analysis. The XRD patterns of CNF and NCNF both exhibit two major peaks at ca. 26° (002) and 43° (100), corresponding to the (002) and (100) planes of crystalline carbon (Fig. 4a) [28–30]. Notably, the carbon reflections of the NCNF ((002) plane) are slightly shifted to smaller 2θ values because of lattice distortion caused by the incorporation of nitrogen atoms [20]. Meanwhile, the relative intensity of the carbon reflections ((100) plane) become weaker upon incorporation of nitrogen atoms, indicating a decrease in the structural order or the formation of defects. As shown in Fig. 4b, the XRD patterns of PtCo/CNF and PtCo/NCNF both display two diffraction peaks at 41.6°and 47.5°, corresponding to the (111) and (200) planes of PtCo alloy nanocrystals, demonstrating the alloy formation between Pt and Co atoms [31–33]. In addition, the PtCo/NCNF treated by NH_3 exhibits relative weaker intensity of (111) and (200) planes of PtCo alloy, demonstrating the smaller sizes of PtCo alloy NP in NCNF than that in CNF. Therefore, the NH_3 can help the CNF to synthesize small sized PtCo alloy during the thermal reduction process, which can also verified by the TEM results in Fig. 1.

To further explore the chemical states and composition, the XPS spectra of PtCo/NCNF are illustrated in Fig. 5. As shown in Fig. 5a, the C 1s spectrum PtCo/NCNF exhibits four fitted peaks with binding energies (BEs) at 284.5, 285.2, 286.3 and 287.8 eV, which are attributed to -C-C, -C-N, -C-OH and -O = C-N groups, respectively [34–36,38]. The existence of -C-N and –O = C-N groups confirms the nitrogen doping into the carbon matrix and, in addition, there are some oxygen groups on the surfaces of the carbon. The high-resolution N 1s XPS spectrum can be fitted to three types of nitrogen species, corresponding to overlapping pyridinic-N (398.7 eV), pyrrolic-N (400.8 eV) and graphitic-N (401.6 eV) [37,39–42], indicating the successful incorporation of nitrogen into the carbon matrix, as shown in Fig. 4c [2,43]. It is well known that both pyridinic-N and graphitic-N are considered potential active sites in the ORR [43]. Fig. 5c displays the Co 2p XPS spectra and the spectra exhibit four peaks at 778.1, 781.7, 793.8 and 802.7 eV, corresponding to the $2p_{3/2}$, $2p_{1/2}$ and their satellite peaks. The peak position of Co $2p_{3/2}$ further corroborate the metallic form of Co. As manifested in Fig. 5d, a doublet in the Pt 4f spectrum of PtCo/NCNF can be identified at approximately 71.8 and 75.1 eV [9,44]. Compared with the BEs of bulk Pt [45],

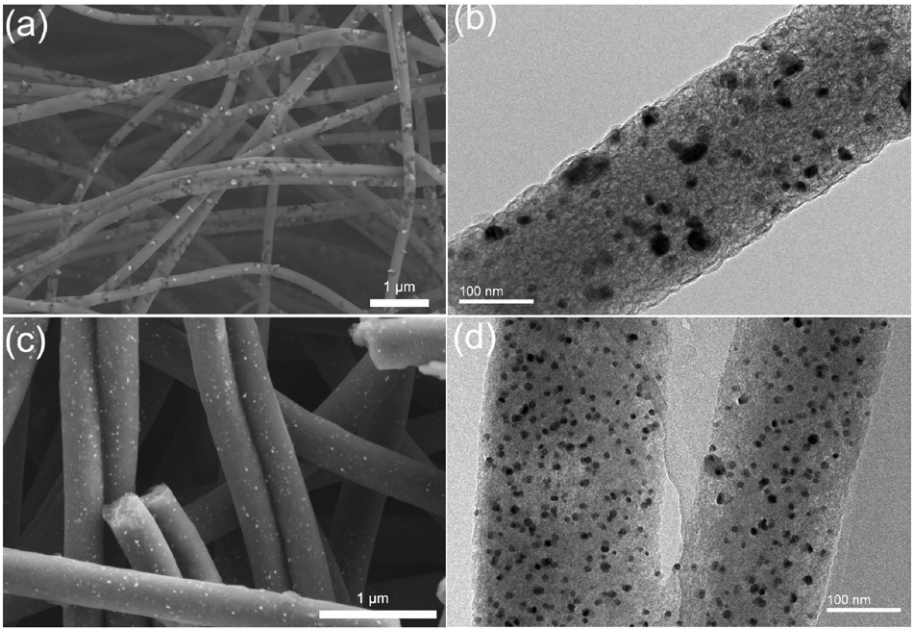

Fig. 2. FESEM and TEM images of the (a, b) Co/CNF and (c, d) PtCo/CNF hybrid nanostructure.

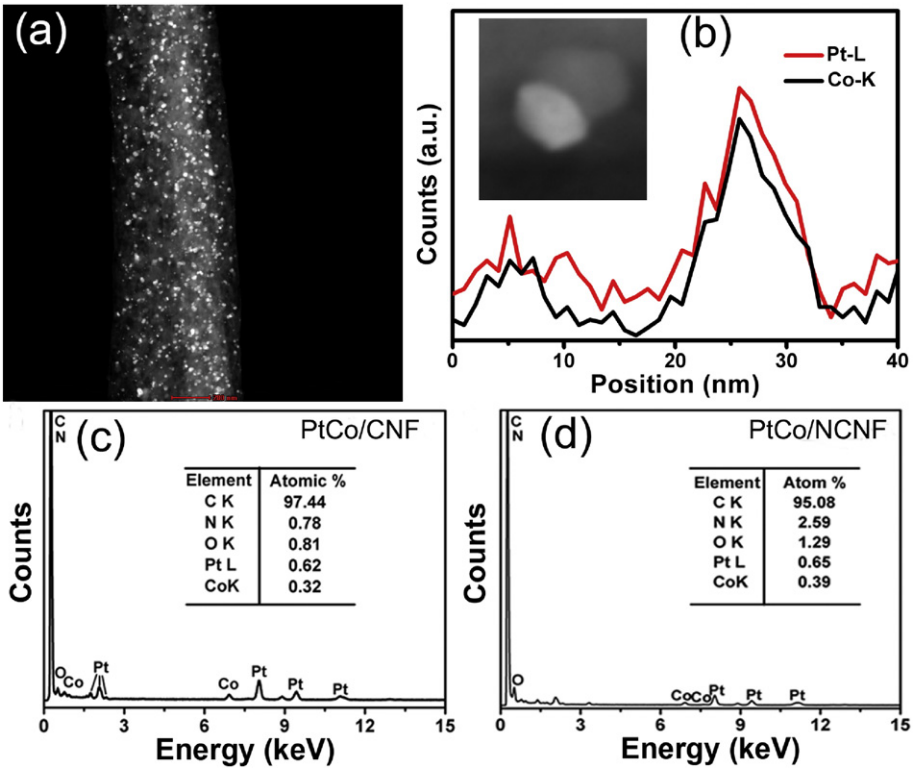

Fig. 3. (a) HAADF-STEM image of PtCo alloy NP in NCNF. (b) Line scan STEM-EDX spectra of PtCo alloy nanocrystal. Inset in (b) is the investigated PtCo alloy NPs. The EDX spectra of (c) PtCo/CNF and (d) PtCo/NCNF hybrid nanostructures.

the BEs of the Pt in PtCo/NCNF shift to relatively higher energy due to the charge transfer from Co to Pt, suggesting the formation of the PtCo alloy structure [2]. All of the above results demonstrate the successful synthesis of the PtCo alloy structure embedded in N-doped CNFs.

The electrocatalytic activity of PtCo/NCNF toward HER and OER on a GCE in an oxygen-free 0.5 M H_2SO_4 and 1 M KOH solution was evaluated using a standard three-electrode system. As a control, similar measurements for CNF, NCNF, Co/CNF, Pt/CNF and PtCo/CNF were also investigated. To minimize the capacitive current, a slow scan rate (1 mV s^{-1}) was applied during the linear sweep voltammetry (LSV) [46]. The electrocatalytic performance of various electrocatalysts for HER were evaluated with a three electrode electrochemical cell in 0.5 M H_2SO_4, as shown in Fig. 6. The NCNF exhibit poor HER activity and the Co/CNF also exhibit weaker HER activity. The Pt/CNF and PtCo/CNF both display lower onset potentials about 52 and 34 mV, and overpotentials at $j =$ 10 mA cm^{-2} of 127 and 68 mV, respectively. Compared with signal phase of Pt/CNF, the PtCo alloy indicate enhanced electrocatalytic activity. The PtCo/NCNF hybrid treated by NH_3 exhibit a low onset potential (20 mV) and a rapidly rising current density with applied potential. It is only required the overpotentials of 50 mV to reach the $j = 10$ mA cm^{-2}. The superior HER performances are better than the commercial Pt/C catalyst (20 wt%) (onset potential of 27 mV and overpotential at $j =$ 10 mA cm^{-2} of 59 mV). The excellent electrocatalytic activity of PtCo/NCNF hybrid is further confirmed by the Tafel slope. As shown in Fig. 6b, the corresponding Tafel slopes for NCNF, Co/CNF, Pt/CNF, PtCo/CNF, PtCo/NCNF and Pt/C catalyst are 193, 169, 55, 30, 30 and 30 mV dec^{-1}, respectively. The PtCo/NCNF exhibit the same Tafel slope of commercial Pt/C catalysts, suggesting the fast electrode kinetics. The very small onset potential and Tafel slope of PtCo/NCNF are better than most of recently reported HER electrocatalysts [46–50].

Stability is another important parameter to evaluate the quality of the HER catalyst. Furthermore, the PtCo alloy NPs might dissolve in the strong acid electrolyte during the potential cycling. As shown in Fig. 6c, after 1000 continuous cyclic voltammetry scans at a scan rate of 100 mV s^{-1} between 0 and 1.2 V vs RHE, the polarization curve of PtCo/NCNF only displays negligible decrease in the onset potentials and current density and remains nearly identical as the initial one. Therefore, the PtCo/NCNF has a long-term stability under the operating

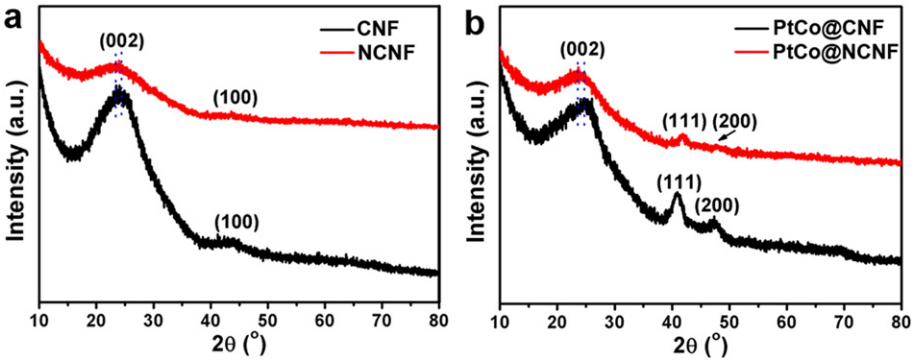

Fig. 4. XRD patterns of (a) CNF and NCNF. XRD patterns of (b) PtCo/CNF and PtCo/NCNF.

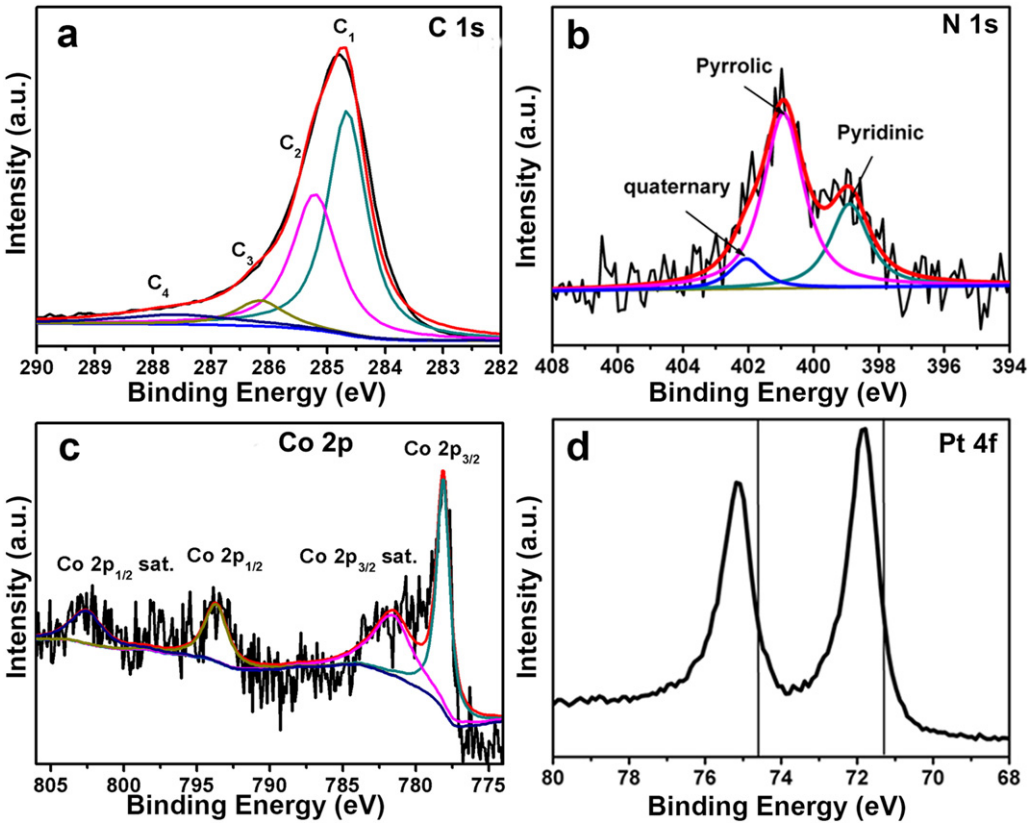

Fig. 5. The high-resolution (a) C 1s, (b) N 1s, (c) Co 2p and (d) Pt 4f XPS spectra of PtCo/NCNF.

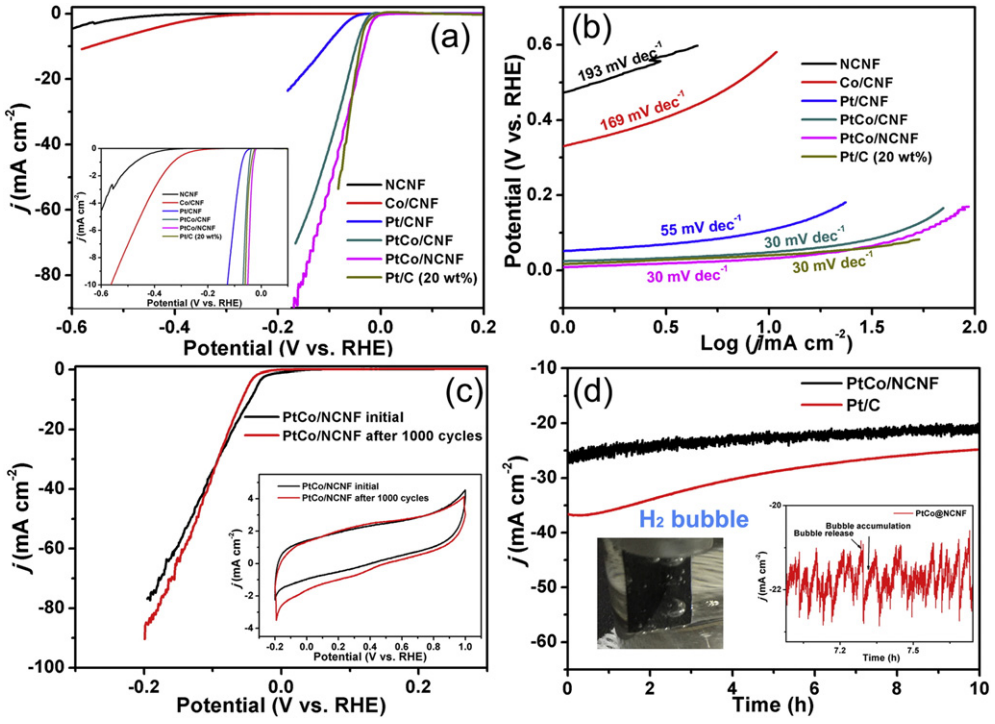

Fig. 6. (a) Polarization curves of NCNF, Co/CNF, Pt/CNF, PtCo/CNF, PtCo/NCNF and commercial Pt/C catalyst (20 wt%) in 0.5 M H_2SO_4 at a potential sweep rate of 1 mV s^{-1}. Inset in (a) is the current density ranged from 0 to 10 mA cm^{-2}. (b) The corresponding Tafel plots of the various electrocatalysts in in 0.5 M H_2SO_4. (c) Polarization curves of the PtCo/NCNF electrode before and after 1000 cycles. Inset in (c) is the CV curves of PtCo/NCNFs before and after 1000 cycles. (d) Chronoamperometric response (*j*-t) recorded on a PtCo/NCNF and Pt/C catalysts electrode at a constant applied potential of −0.3 V vs RHE. The PtCo/NCNF membrane was directly used as the working electrode. Inset in (d) is the optical image of PtCo/NCNFs membrane electrode operating at −0.3 V with generated H_2 bubbles on the surface.

conditions medium to withstand accelerated degradation, mainly due to the unique core-shell of PtCo and carbon and protection of carbon layers from corrosion.

The PtCo/NCNF were directly used as the electrode to investigate the durability at a constant potential of −0.3 V vs RHE in 0.5 M H_2SO_4 solution by chronoamperometric measurements (Fig. 6d). The PtCo/NCNF membrane show a good level of stability with small current density decrease during 10 h continuous constant-potential electrolysis. In comparison, after 10 h operation, the current density of Pt/C catalyst exhibit 30% decrease, which are larger than that of PtCo/NCNF. It is seen that large amounts of H_2 bubbles were generated on the surfaces of PtCo/NCNF membrane during the continuous electrolysis, as shown in inset in Fig. 6d. The H_2 bubble accumulation and bubble release process on the surfaces of PtCo/NCNFs membrane was also given in inset in Fig. 6d. The durable HER performance indicated that the PtCo/NCNF membrane are stable and practical electrocatalysts for HER.

The electrocatalytic performances of various catalysts for OER are shown in Fig. 7. As expected, the PtCo/NCNF and PtCo/CNF both show relatively high OER activity, whereas NCNF and CNF show negligible OER performance. A potential of 1.64 V for the PtCo/NCNF catalyst is required to achieve a j (vs RHE) of 10 mA cm^{-2}, which is a smaller value than that of PtCo/CNF catalyst (1.74 V). As control, the Pt/C (20 wt%) catalysts need a potential of 1.76 V to achieve a j (vs RHE) of 10 mA cm^{-2}, which is larger than that of PtCo/NCNF catalysts, indicating the better OER activity of PtCo/NCNFs. The PtCo/NCNF possess high nitrogen contents (2.59 wt%) than that of PtCo/CNF (0.78 wt%). It is noted that the PtCo/NCNF shows higher OER activity than PtCo/CNF, highlighting the critical role of the type of N-doping on OER activity. However, the pure NCNF and CNF could not reach a j of 10 mA cm^{-2}, implying poor OER performances. The Tafel slopes of PtCo/NCNF, PtCo/CNF and Pt/C (20 wt%) were 76, 83 and 155 mV dec^{-1}, respectively, as shown in Fig. 7b. The interaction between encapsulated PtCo alloy NPs and the surrounding N-doped carbon layer are beneficial for OER activity [51].

In addition to good catalytic activity, durability is another significant criterion for evaluating practical applications. Moreover, particle aggregation is prone to occur during the potential cycling under a strong alkaline electrolyte. As shown in Fig. 7d, after 1000 continuous cyclic voltammetry scans at a scan rate of 100 mV s^{-1} between 0 and 1.2 V vs RHE, the polarization curve of PtCo/NCNF remains nearly identical as the initial one. Moreover, only a negligible current density loss was observed during the potential cycling. The PtCo/NCNF electrode has long-term viability under the operating conditions medium to withstand accelerated degradation, mainly as a result of the encapsulation structure protection of PtCo alloy NPs from corrosion.

The PtCo/NCNF membrane was directly used as the working electrode for the OER catalyst and the durability at a constant potential of 1.64 V vs RHE in 1 M KOH solution was tested by chronoamperometric measurements (Fig. 7c). The current density of PtCo/NCNF exhibits negligible degradation after continuous operation for 10 h, indicating that the PtCo/NCNF membrane can be directly used as an electrode for practical applications under alkaline conditions. Meanwhile, the Pt/C catalysts exhibit much degrease in the current density after the continuous operation for 10 h. The morphologies of PtCo/NCNF membrane after stability test for 10 h in 0.5 M H_2SO_4 and in 1 M KOH were shown in Fig. 8. No matter what the PtCo/NCNF membrane used in acid or alkaline solution for long time, the size and well dispersion of PtCo alloy in NCNF did not dissolve or grow up to larger sizes, suggesting the strong protection from the acid and alkaline solution. Based on the above results, the PtCo/NCNF is expected to be a promising OER catalyst.

The superior catalytic performance of PtCo/NCNF in overall water splitting are ascribed to the synergistic effects of the small and well-dispersed PtCo alloy carbon core-shell structures, high conductivity of NCNF and N-doped carbon. The interconnected 3D NCNF architecture acted as an interconnected conducting network and afforded the growth of highly dispersed PtCo alloy NPs. Benefiting from the unique 3D membrane structures, the reaction kinetics of both the HER and

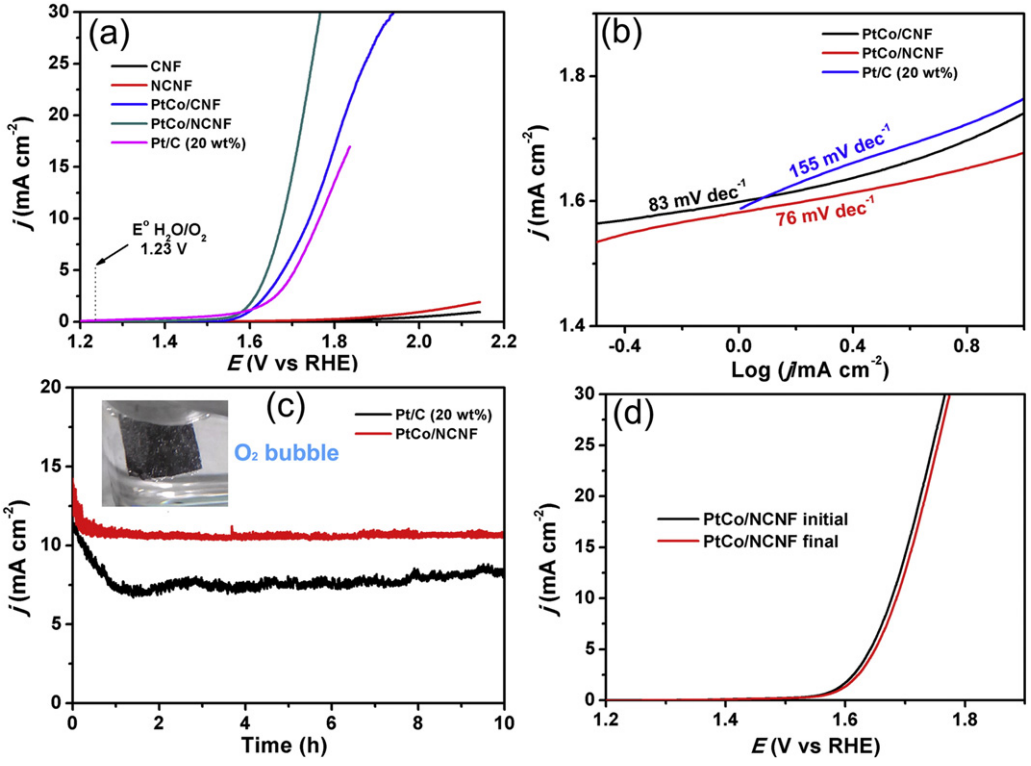

Fig. 7. (a) Polarization curves of CNF, NCNF, PtCo/CNF and PtCo/NCNF, Pt/C catalyst (20 wt%) at a potential sweep rate of 1 mV s^{-1}. (b) Tafel plots of PtCo/CNF and PtCo/NCNF in 1 M KOH solution. (c) Chronoamperometric response (j-t) recorded on PtCo/NCNF and Pt/C catalyst (20 wt%) membrane electrode at a constant applied potential of 1.64 V vs RHE. The PtCo/NCNF catalyst was directly used as the working electrode. Inset in (c) is the optical image of PtCo/NCNFs membrane electrode operating at 1.64 V with generated O_2 bubbles on the surface. (d) Polarization curves of the PtCo/NCNF membrane electrode before and after 1000 potential cycles (scan rate: 100 mV s^{-1}).

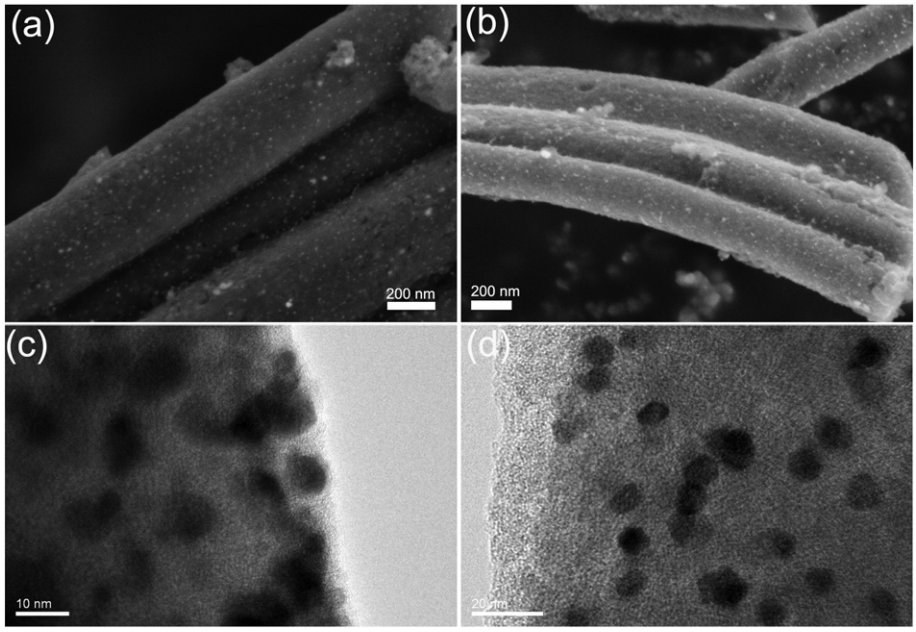

Fig. 8. The FE-SEM and TEM images of the morphology of the PtCo/NCNF membrane after stability test for 10 h in (a, c) 0.5 M H_2SO_4 and (b, d) in 1 M KOH.

OER are significantly promoted. The 3D structure constructed by the well-defined and interwoven 1D NCNF provide smooth pathways to facilitate penetration of the electrolyte and enlarge the contact surface between reactants and active sites [52–54]. Furthermore, the 3D hierarchical structures also enables facile release of evolved gas bubbles to further improve the reaction interface. The introduction of Co into PtCo alloy NPs changed the electronic structure of Pt to maintain more free and Pt active sites for electrocatalytic activity [55,56]. Small sizes and well-dispersed PtCo alloy provide a large active surface area, which facilitates diffusion of active species and accelerates subsequent surface electrochemical reactions. The PtCo alloy NPs encapsulated in N-doped carbon shells enabled rapid electron transport from the NPs to the electrodes and also impeded the metal NPs dissolution in acid and alkaline electrolyte [57]. The dopant atom in carbon not only promoted electron transfer but also provided more active sites for OER, especially the pyridinic and quaternary N atoms.

4. Conclusions

In summary, carbon nanofibers served as nanoreactors for the design and construction of PtCo alloy NPs encapsulated in N-doped carbon shells through a combination of electrospinning and nitrogen doping treatments. Small sized PtCo alloy carbon core-shell nanoparticles were uniformly dispersed throughout the whole CNF. The PtCo/NCNF hybrid consists of PtCo alloy nanoparticles surrounded by a few of N-doped carbon layers, demonstrating a typical core-shell structures. The PtCo/NCNF hybrid can both served as electrode materials for HER and OER. For the HER performance, the PtCo/NCNF exhibit very small onset potential of 20 mV, overpotentials at a j (vs RHE) of 10 mA cm^{-2} of 50 mV and Tafel slope of 30 mV dec^{-1}, which are better than the commercial Pt/C (20 wt%) and PtCo/CNF catalysts. In addition, the PtCo/NCNF hybrid also exhibits high OER activity with an onset potential of 310 mV, an overpotential of 410 mV at a j of 10 mA cm^{-2} and a small Tafel slope of 76 mV dec^{-1}. The high catalytic activities of PtCo alloy for HER and OER originate from the 3D hierarchical structures, well-dispersed PtCo alloy, high conductivity of CNF, protection from the carbon-encapsulated structure, and the introduction of nitrogen.

Acknowledgements

This study was supported by the National Natural Science Foundation of China (NSFC) (Grant no. 51373154, 51573166) and the Natural Science Foundation of Zhejiang Province (Grant No. LQ16E020005).

References

[1] H. Jin, J. Wang, D. Su, Z. Wei, Z. Pang, Y. Wang, J. Am. Chem. Soc. 137 (2015) 2688.
[2] W. Zhou, J. Zhou, Y. Zhou, J. Lu, K. Zhou, L. Yang, Z. Tang, L. Li, S. Chen, Chem. Mater. 27 (2015) 2026.
[3] F. Song, X. Hu, J. Am. Chem. Soc. 136 (2014) 16481.
[4] F. Jiao, H. Frei, Angew. Chem. Int. Ed. 48 (2009) 1841.
[5] D.M. Robinson, Y.B. Go, M. Mui, G. Gardner, Z. Zhang, D. Mastrogiovanni, E. Garfunkel, J. Li, M. Greenblatt, G.C. Dismukes, J. Am. Chem. Soc. 135 (2013) 3494.
[6] D. Delgado, M. Minakshi, J. McGinnity, D.J. Kim, Sci. Rep. 5 (2015) 15208.
[7] B.Y. Xia, Y. Yan, N. Li, H.B. Wu, X.W. Lou, X. Wang, Nat. Energy 1 (2016) 1.
[8] X. Liu, W. Liu, M. Ko, M. Park, M.G. Kim, P. Oh, S. Chae, S. Park, A. Casimir, G. Wu, J. Cho, Adv. Funct. Mater. 25 (2015) 5799.
[9] J. Xiao, L. Wan, X. Wang, Q. Kuang, S. Dong, F. Xiao, S. Wang, J. Mater. Chem. A 2 (2014) 3794.
[10] P.W. Menezes, A. Indra, D. Gonzalez-Flores, N.R. Sahraie, I. Zaharieva, M. Schwarze, P. Strasser, H. Dau, M. Driess, ACS Catal. 5 (2015) 2017.
[11] X. Ge, Y. Liu, F.W. Thomas Goh, T.S. Andy Hor, Y. Zong, P. Xiao, Z. Zhang, S.H. Lim, B. Li, X. Wang, Z. Liu, ACS Appl. Mater. Interfaces 6 (2014) 12684.
[12] Y. Gorlin, T.F. Jaramillo, J. Am. Chem. Soc. 132 (2010) 13612.
[13] Y. Liang, Y. Li, H. Wang, J. Zhou, J. Wang, T. Regier, H. Dai, Nat. Mater. 10 (2011) 780.
[14] Z. Wang, S. Xiao, Z. Zhu, X. Long, X. Zheng, X. Lu, S. Yang, ACS Appl. Mater. Interfaces 7 (2015) 4048.
[15] T. Yang, H. Zhu, M. Wan, L. Dong, M. Zhang, M. Du, Chem. Commun. 52 (2016) 990.
[16] H. Zhu, J.F. Zhang, R.P. Yanzhang, M.L. Du, Q.F. Wang, G. Gao, J. Wu, G. Wu, M. Zhang, B. Liu, J.M. Yao, X.W. Zhang, Adv. Mater. 27 (2015) 4752.
[17] H. Zhu, F.L. Lyu, M.L. Du, M. Zhang, Q.F. Wang, J.M. Yao, B.C. Guo, ACS Appl. Mater. Interfaces 6 (2014) 22126.
[18] M.L. Zou, J.D. Chen, L.F. Xiao, H. Zhu, T.T. Yang, et al., J. Mater. Chem. A 3 (2015) 18090.
[19] Q. Liu, Y. Wang, L. Dai, J. Yao, Adv. Mater. (2016), http://dx.doi.org/10.1002/adma.201506112.
[20] A. Zhao, J. Masa, W. Xia, A. Maljusch, M.-G. Willinger, G. Clavel, K. Xie, R. Schlögl, W. Schuhmann, M. Muhler, J. Am. Chem. Soc. 136 (2014) 7551.
[21] J. Yang, H. Sun, H. Liang, H. Ji, L. Song, C. Gao, H. Xu, Adv. Mater. (2016), http://dx.doi.org/10.1002/adma.201505855.
[22] Y. Qiu, G. Li, Y. Hou, Z. Pan, H. Li, W. Li, M. Liu, F. Ye, X. Yang, Y. Zhang, Chem. Mater. 27 (2015) 1194.
[23] Y. Liang, H. Wang, P. Diao, W. Chang, G. Hong, Y. Li, M. Gong, L. Xie, J. Zhou, J. Wang, T.Z. Regier, F. Wei, H. Dai, J. Am. Chem. Soc. 134 (2012) 15849.
[24] L. Zhou, P. Fu, X. Cai, S. Zhou, Y. Yuan, Appl. Catal. B Environ. 188 (2016) 31.
[25] D. Dontsova, S. Pronkin, M. Wehle, Z. Chen, C. Fettkenhauer, G. Clavel, M. Antonietti, Chem. Mater. 27 (2015) 5170.

[26] R.V. Jagadeesh, H. Junge, M. Beller, Nat. Commun. 5 (2014) 4123.
[27] Z. Hu, J.C. Yu, J. Mater. Chem. A 1 (2013) 12221.
[28] S. Yuan, X. Dai, Green Chem. (2016), http://dx.doi.org/10.1039/c5gc02729b.
[29] X. Yang, Y. Yu, N. Yan, H. Zhang, X. Li, H. Zhang, J. Mater, Chem. A (2016), http://dx.doi.org/10.1039/c6ta01060a.
[30] J. Hou, C. Cao, F. Idrees, X. Ma, ACS Nano 9 (2015) 2556.
[31] D. Wang, H.L. Xin, R. Hovden, H. Wang, Y. Yu, D.A. Muller, F.J. DiSalvo, H.D. Abruña, Nat. Mater. 12 (2013) 81.
[32] A.S. Arico, A. Stassi, I. Gatto, G. Monforte, E. Passalacqua, V. Antonucci, J. Phys. Chem. C 114 (2010) 15823.
[33] S. Choi, S. Lee, W.Y. Kim, R. Choi, K. Hong, K.M. Nam, S.W. Han, J.T. Park, ACS Appl. Mater. Interfaces 4 (2012) 6228.
[34] Q. Wang, R. Yanzhang, Y. Wu, H. Zhu, J. Zhang, M.L. Du, M. Zhang, L. Wang, X. Zhang, X. Liang, RSC Adv. 6 (2016) 34219.
[35] M. Li, Y. Xiong, X. Liu, C. Han, Y. Zhang, X. Bo, L. Guo, J. Mater. Chem. A 3 (2015) 9658.
[36] Z. Wang, S. Xiao, Z. Zhu, X. Long, X. Zheng, X. Lu, S. Yang, ACS Appl. Mater. Interfaces 7 (2015) 4048.
[37] V. Datsyuk, M. Kalyva, K. Papagelis, J. Parthenios, D. Tasis, A. Siokou, I. Kallitsis, C. Galiotis, Carbon 46 (2008) 833.
[38] Z. Chen, A. Yu, R. Ahmed, H. Wang, H. Li, Z. Chen, Electrochim. Acta 69 (2012) 295.
[39] R.M. Yadav, J. Wu, R. Kochandra, L. Ma, C.S. Tiwary, L. Ge, G. Ye, R. Vajtai, J. Lou, P.M. Ajayan, ACS Appl. Mater. Interfaces 7 (2015) 11991.
[40] D. Guo, R. Shibuya, C. Akiba, S. Saji, T. Kondo, J. Nakamura, Science 351 (2016) 361.
[41] H. Ba, Y. Liu, L. Truong-Phuoc, C. Duong-Viet, J. Nhut, D. Lam Nguyen, O. Ersen, G. Tuci, G. Giambastiani, C. Pham-Huu, ACS Catal. 6 (2016) 1408.
[42] J. Wang, D. Gao, G. Wang, S. Miao, H. Wu, J. Li, X. Bao, J. Mater. Chem. A 2 (2014) 20067.
[43] Y. Vasquez, A.K. Sra, R.E. Schaak, J. Am. Chem. Soc. 127 (2005) 12504.
[44] T. Yang, M. Du, H. Zhu, M. Zhang, M. Zou, Electrochim. Acta 167 (2015) 48.
[45] T.Y. Ma, S. Dai, M. Jaroniec, S.Z. Qiao, J. Am. Chem. Soc. 136 (2014) 13925.
[46] J. Xu, J. Cui, C. Guo, Z. Zhao, R. Jiang, S. Xu, Z. Zhuang, Y. Huang, L. Wang, Y. Li, Angew. Chem. Int. Ed. (2016), http://dx.doi.org/10.1002/anie.201600686.
[47] N. Ma, Y. Jia, X. Yang, X. She, L. Zhang, Z. Peng, X. Yao, D. Yang, J. Mater, Chem. A (2016), http://dx.doi.org/10.1039/c6ta00591h.
[48] Y. Jin, H. Wang, J. Li, X. Yue, Y. Han, P.K. Shen, Y. Cui, Adv. Mater. (2016), http://dx.doi.org/10.1002/adma.201506314.
[49] H. Fei, Y. Yang, Z. Peng, G. Ruan, Q. Zhong, L. Li, E.L.G. Samuel, J.M. Tour, ACS Appl. Mater. Interfaces 7 (2015) 8083.
[50] Z. Li, S. Shi, Q. Zhong, C. Zhang, C. Xu, Electrochim. Acta 146 (2014) 119.
[51] M. Gao, X. Cao, Q. Gao, Y. Xu, Y. Zheng, J. Jiang, S. Yu, ACS Nano 8 (2014) 3970.
[52] Z. Li, F. Wang, A. Kvit, X. Wang, J. Phys. Chem. C 119 (2015) 4397.
[53] P. Pathak, S. Gupta, K. Grosulak, H. Imahori, V. Subramanian, J. Phys. Chem. C 119 (2015) 7543.
[54] X. Zhao, J. Zhang, L. Wang, H.X. Li, Z. Liu, W. Chen, ACS Appl. Mater. Interfaces 7 (2015) 26333.
[55] P.J. Dietrich, M.C. Akatay, F.G. Sollberger, E.A. Stach, J.T. Miller, W.N. Delgass, F.H. Ribeiro, ACS Catal. 4 (2014) 480.
[56] P.C. Chen, G. Liu, Y. Zhou, K.A. Brown, N. Chernyak, J.L. Hedrick, S. He, Z. Xie, Q.Y. Lin, V.P. Dravid, S.A. O'Neill-Slawecki, C.A. Mirkin, J. Am, Chem. Soc. 137 (137) (2015) 9167.
[57] H. Fei, Y. Yang, Z. Peng, G. Ruan, Q. Zhong, L. Li, E.L.G. Samuel, J.M. Tour, ACS Appl. Mater. Interfaces 7 (2015) 8083.